Exp Brain Res (2011) 214:515–528
DOI 10.1007/s00221-011-2850-5

RESEARCH ARTICLE

Anatomically constrained minimum variance beamforming applied to EEG

Vyacheslav Murzin · Armin Fuchs · J. A. Scott Kelso

Received: 17 September 2010 / Accepted: 20 August 2011 / Published online: 14 September 2011

Abstract Neural activity as measured non-invasively using electroencephalography (EEG) or magnetoencephalography (MEG) originates in the cortical gray matter. In the cortex, pyramidal cells are organized in columns and activated coherently, leading to current flow perpendicular to the cortical surface. In recent years, beamforming algorithms have been developed, which use this property as an anatomical constraint for the locations and directions of potential sources in MEG data analysis. Here, we extend this work to EEG recordings, which require a more sophisticated forward model due to the blurring of the electric current at tissue boundaries where the conductivity changes. Using CT scans, we create a realistic three-layer head model consisting of tessellated surfaces that represent the cerebrospinal fluid-skull, skull-scalp, and scalp-air boundaries. The cortical gray matter surface, the anatomical constraint for the source dipoles, is extracted from MRI scans. EEG beamforming is implemented on simulated sets of EEG data for three different head models: single spherical, multi-shell spherical, and multi-shell realistic. Using the same conditions for simulated EEG and MEG data, it is shown (and quantified by receiver operating characteristic analysis) that EEG beamforming detects radially oriented sources, to which MEG lacks sensitivity. By merging several techniques, such as linearly constrained minimum variance beamforming, realistic geometry forward solutions, and cortical constraints, we demonstrate it is possible to localize and estimate the dynamics of dipolar and spatially extended (distributed) sources of neural activity.

Keywords Electroencephalography · EEG · Source reconstruction · Inverse problem · Beamforming · Boundary element method

V. Murzin (✉) · A. Fuchs · J. A. S. Kelso
Center for Complex Systems and Brain Sciences,
Florida Atlantic University, Boca Raton, FL 33431, USA
e-mail: murzin@ccs.fau.edu

A. Fuchs
Physics Department, Florida Atlantic University,
Boca Raton, FL 33431, USA

J. A. S. Kelso
Intelligent Systems Research Centre,
University of Ulster, Derry, Northern Ireland, UK

Introduction

Non-invasive techniques such as electroencephalography (EEG), magnetoencephalography (MEG), magnetic resonance imaging (MRI), functional MRI (fMRI), positron emission tomography (PET), and computed tomography (CT) provide complementary measures of structure, function, and dynamics of the living human brain and have proved essential for scientific research and clinical diagnostics. The zoo of imaging technologies is based on different physical principles and exploits different tissue properties and physiological responses. MRI and fMRI measure the level of water and the hemodynamic response (changes in blood flow and level of oxygen in the blood due to both intrinsic and task-induced properties of the brain), respectively. The neural sources in the brain produce electric currents whose effects can be measured in the form of magnetic fields outside the head (MEG) or electric potentials on the scalp surface (EEG). These measurements have the common primary goal of estimating the locations of neural activity inside the brain. Functional MRI, when compared to M/EEG, offers real 3-D imaging with high spatial resolution but due to the nature of the hemodynamic

response has very limited temporal resolution. In contrast, M/EEG measures changes in electric and magnetic fields with a sampling rate of 1,000 Hz. Typical brain activity of interest ranges from 0.1 to 100 Hz (Nunez and Srinivasan 2006) even though the actual frequency range is much larger. The main problem is to find the locations and directions of the neural sources inside the brain from electric potentials or magnetic fields measured on the outside of the head. This so-called inverse problem cannot be solved uniquely (von Helmholtz 1853) because infinitely many source configurations can lead to the same potential or magnetic field readings at the sensors.

Various approaches have been developed to obtain inverse solutions by means of estimating neural activity from M/EEG measurements. These include minimum norm estimation (Gorodnitsky et al. 1992), dipole source analysis/localization (DSL), which is implemented in commercially available software packages, multiple signal classification (MUSIC) (Mosher et al. 1992), independent component analysis (ICA) (Delorme and Makeig 2004), Lead-field-based imaging (Hämäläinen and Ilmoniemi 1994), and beamforming (van Veen et al. 1997; Robinson and Vrba 1999).

Beamforming is a signal processing technique based on the calculation of the covariance between signals at different sensors, leading to sensor weights such that the array becomes most sensitive to a certain location and direction inside a volume, yet at the same time suppressing interference from all other locations. Beamforming was initially developed for radio and sound waves (Frost III 1972; Borgiotti and Kaplan 1979) and was later used for MEG source localization (van Veen and Buckley 1988; Sekihara 1996; Robinson and Vrba 1999; Cheyne and Gaetz 2003; Cheyne et al. 2006). Application of beamforming to EEG has also been reported (Spencer et al. 1992; Ward et al. 1998; van Hoey et al. 1999; Brookes et al. 2008; Wong and Gordon 2009).

Originally, MEG beamforming scanned the whole brain or a region of interest on a grid of a certain size, where the sources were assumed to be at the nodes of the grid, leading to a 5 degree of freedom (dof) task: 3 dof for the location and 2 for the direction of the source. This dimensionality can be significantly reduced if anatomical constraints are taken into account. It is well known that most of the signals picked up by EEG or MEG are produced by simultaneous activation of tens of thousands of neurons (Nunez and Srinivasan 2006) acting coherently in the cortical gray matter (Braitenberg and Schüz 1991). Furthermore, the pyramidal cells in the gray matter form cell bundles, the macrocolumns, oriented perpendicular to the surface. Taking these facts together, anatomically constrained beamforming assumes all sources confined to the cortical surface with a direction perpendicular to it as shown in Fig. 1.

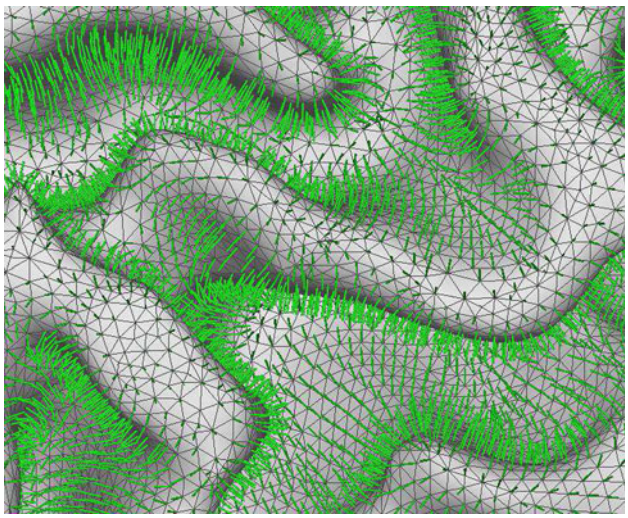

Fig. 1 Dipoles representing neural activity sources for anatomically constrained beamforming are assumed to be located on the cortical surface with the direction perpendicular to the surface

Here, we provide a detailed workflow of high-resolution linearly constrained minimum variance (LCMV) beamforming with the cortex as an anatomical constraint, adaptable to spherical and realistic forward solutions. The novelty and potential significance of our approach is in the combination of several well established techniques in a way that has not been previously considered for source localization using EEG. Moreover, the developed method, while based on simulated EEG data, allows for comparison of different forward solutions, comparison of EEG and MEG, and for testing different dipole source configurations including spatially extended regions (patches) of activity.

Inverse problem and forward solutions

Estimating source currents from observations of electromagnetic activity outside the brain is known as an inverse problem. Such problems are generally ill-posed and cannot be solved uniquely (von Helmholtz 1853). However, there are methods that allow for finding locations of neural activity with fairly good resolution, e.g., dipole source localization, multiple signal classification, and, more recently, beamforming. An accurate forward solution is a required prerequisite for beamforming that essentially calculates the overlap between the measured and expected (theoretical) signal at the sensors.

An electromagnetic forward solution assumes a current dipole (or a finite set of them) inside a volume and provides the electric potential and/or magnetic field at the points of interest (sensors). The magnetic field is not affected when penetrating the various tissues inside the head, as their relative permeability is $\mu/\mu_0 \cong 1$ and can be calculated

straightforwardly. In contrast, the propagation of the electric field (electric potential) depends on the conductivity of the tissue and is greatly reduced and smeared at boundaries between different tissue types. The conductivity of the skull is about 100 times smaller than the conductivity of the cerebrospinal fluid (CSF) and skin and therefore cannot be neglected in the EEG forward solution. The EEG forward solution is also affected by the shape of the tissue layer.

For comparison we consider three different head models: a single homogeneous sphere of constant conductivity, a 3-layer concentric sphere model where the conductivity of each layer is taken into account, and a 3-layer model that is not restricted to a spherical shape and utilizes the real geometry of the head created from a CT and MRI scan of the subject. The explicit formulations and mathematical details are given in "Appendix 2".

The forward solution for a dipole is represented by **G**, a multidimensional (dimensionality given by the number of sensors) vector of values of electric potential or magnetic field strength at the sensors. The norm of this vector we call the magnitude of the forward solution |**G**|. EEG and MEG are complementary in the sense that |**G**| is different for sources at different locations on the cortical surface. The magnitude of the magnetic forward solution |**G**| calculated using the spherical model (Appendix 1) everywhere on the cortical surface is shown in Fig. 2a. The walls of sulci are red to bright yellow, representing a high magnitude of the forward solution. Plotted in light blue are the values close to zero, which means that dipoles that are radial (i.e., top of gyri) produce a much weaker signal at the sensors. In contrast, the electroencephalogram is sensitive to both radial and tangential sources as shown in Fig. 2b. Moreover, EEG is most sensitive to the radial sources located on top of the gyri, because these sources generate a stronger and more focused electric potential at the scalp.

Anatomy of the human head and surface extraction

Though human brains have structural similarities across different subjects, variations in volume, shape of the head, and complexity of the cortical folds make every brain unique. In addition, the shape of the skull is also unique. Therefore, to accurately estimate the neural activity in electroencephalography, both, anatomical (such as the cortical surface and skull/skin interfaces) and electrophysiological data must be obtained from the same subject.

The EEG forward solution model (Stok et al. 1987; Mosher et al. 1999) used in the present paper (described in details in "Multi-shell case (realistic geometry)") assumes a multi-shell head model constructed from the cortical surface, CSF, skull, and scalp. Attenuation and smearing of the EEG signal happens at the interfaces between layers with different conductivities, primarily at the skull-scalp interface (Nunez and Srinivasan 2006). The thickness of the skull in different regions of the head is also important. One way to obtain the head surfaces is to use computed tomography (CT). The CT scan shows bone bright and easily recognizable (Fig. 3b) compared to an MRI scan (Fig. 3a), where the bone appears diffusely dark. Therefore, CT is more reliable for identifying bone structure. Moreover, even though automated scripts like "Freesurfer" (Dale et al. 1999; Fischl et al. 1999) can give an estimate of the inner and outer bone surfaces, we chose to create our own tessellation because it allowed for more flexible control over certain regions, like the bottom of the head. The skin surface, also extracted from the CT scan, serves as a constraint for the EEG electrode locations.

The resulting surface tessellations (648 vertices each) of the CSF (blue), skull (yellow), and skin (red) are shown in Fig. 4. The bottom of each surface is closed artificially to satisfy the BEM requirement of closed surfaces and at the same time to have the gray matter fully inside the CSF volume. This construction and tesselation size of 648 vertices are justified by the fact that we are interested only in the electric potential interpolated at 122 EEG sensor locations shown as green dots overlaying the scalp surface. The brain surface or gray-white matter boundary (shown in gray in Fig. 4) is obtained using the software package "Freesurfer" and consists of approximately 284,000 vertices and 568,000 triangles.

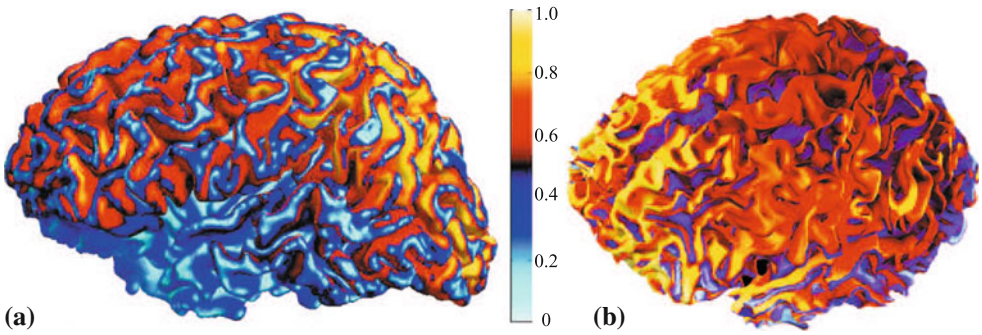

Fig. 2 MEG (**a**) and EEG (**b**) forward solution magnitudes plotted on the cortical surface. Normalized relative magnitudes depend on dipole source location and direction. *Yellow* indicates high values, *cyan* indicates values close to zero

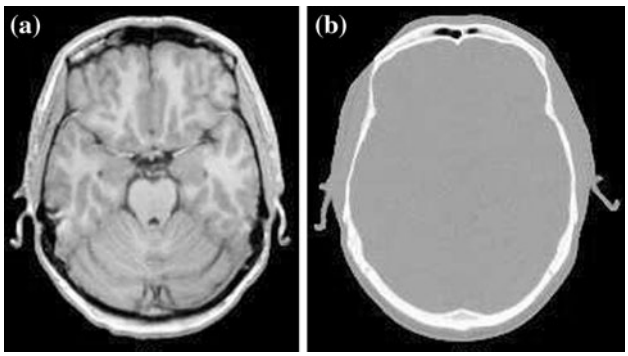

Fig. 3 MRI scan (**a**) provides the brain tissue structure, CT scan (**b**) can be used to extract the skull and scalp surfaces

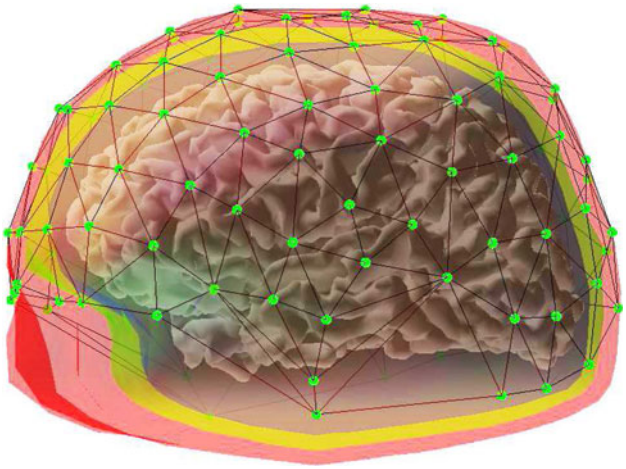

Fig. 4 Head surfaces constructed from MRI and CT scans (*red* scalp, *yellow* skull, *blue* CSF, *gray* gray matter). EEG electrodes are shown as green dots

EEG beamforming: simulations

In a first step, we apply the beamforming method[1] to EEG from a single dipole source, patterns of which are shown in Fig. 5. This dataset (as for all simulated EEG datasets in this study) is created by activating a certain electric dipole (or a set of them) with a time course, for instance, a damped oscillator function. In order to make the simulated data more realistic, two types of noise are added onto the source and its environment (the rest of the brain). For the former, white noise of 14 dB is added to the dipole moment amplitude, whereas the latter is implemented by activating a randomly chosen set of 100 dipoles at each time step. The dataset is obtained by using the superposition principle of electric fields, which allows to merge the forward solutions from the source dipoles with the forward solutions of the randomly activated currents. The signal-to-noise ratio in our simulations is defined as $20\log\frac{A_S}{A_N}$, where A_S and A_N are the amplitudes of the signal and the noise respectively and was kept in the range of 12–16 dB.

Calculation of the neural activity index N_a and reconstructed time series $X_\Theta^{\mathrm{rec}}(t)$ starts with the covariance matrix $\mathbf{C}$, the components of which are

$$C_{ij} = \frac{1}{T}\int_0^T X_i(t)X_j(t)\mathrm{d}t \tag{1}$$

where $X_i(t)$ is the time series at the ith EEG electrode.

In order to calculate the beamformer weights $\mathbf{H}_\Theta$ we need the inverse of the covariance matrix $\mathbf{C}^{-1}$ and the forward solutions $\mathbf{G}_\Theta$ from all locations Θ on the cortical surface. The latter is pre-calculated for different head models and the former requires the addition of a regularization parameter to the diagonal in order to be invertible. The beamformer weights are then obtained from

$$\mathbf{H}_\Theta = \frac{\mathbf{C}^{-1}\mathbf{G}_\Theta}{\mathbf{G}_\Theta \cdot \mathbf{C}^{-1}\mathbf{G}_\Theta} \tag{2}$$

and the neural activity index N_a is calculated as

$$N_a = \frac{\mathbf{G}_\Theta \cdot \mathbf{C}^{-1}\mathbf{G}_\Theta}{\mathbf{G}_\Theta \cdot \mathbf{C}^{-1}\Sigma\mathbf{C}^{-1}\mathbf{G}_\Theta} \tag{3}$$

where $\mathbf{\Sigma}$ is the noise covariance matrix. The reconstructed time series reads

$$X_\Theta^{rec}(t) = \mathbf{X}(t)\cdot\mathbf{H}_\Theta \tag{4}$$

where $\mathbf{H}_\Theta$ are the beamformer weights calculated for the location and direction Θ and $\mathbf{X}(t)$ is the EEG signal at the electrodes.

An example of a beamformer reconstruction of neural activity is shown in Fig. 6. We consider a source dipole placed in the left hemisphere on the white matter surface at location Θ with a direction perpendicular to that surface. The source is given a time series $X_\Theta^{\mathrm{orig}}(t)$ (middle)—a damped oscillator with additive white noise. The hemispheres in Fig. 6 are arranged in a continuous fashion (from left to right: left hemisphere is anterior-to-posterior, right hemisphere is posterior-to-anterior) such that the bottom graph, representing the neural activity index N_a in arbitrary units, is plotted as a function of the longitudinal coordinate of the vertices on the cortical surface of a given hemisphere. The threshold for the values of N_a when plotted on the cortical surface is the average of N_a plus three standard deviations ($\bar{N}_a + 3\sigma$).

Visual inspection of the graph of the neural activity index in Fig. 6 (bottom) allows us to determine the number and approximate location of regions with a signal strength significantly larger than the mean activity of the rest of the brain. It also gives an estimate of the signal-to-noise ratio

[1] For explicit formulations see "Appendix 3".

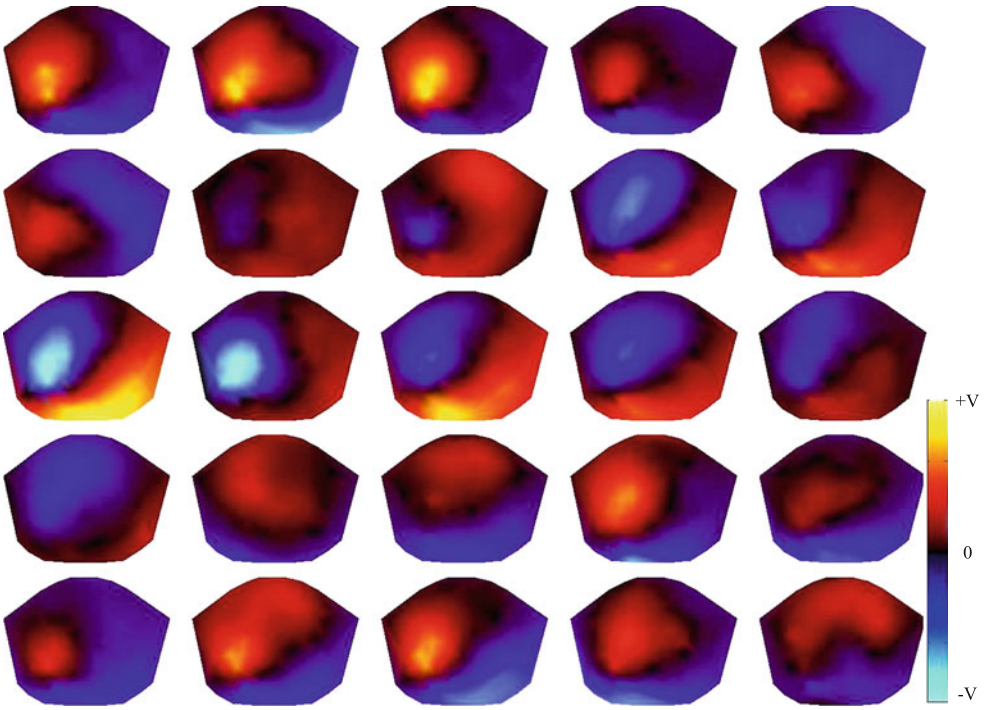

Fig. 5 Simulated EEG patterns: single dipole source located in the left hemisphere as shown in Fig. 6. Time steps (arbitrary scale) run from top *left* to bottom *right*

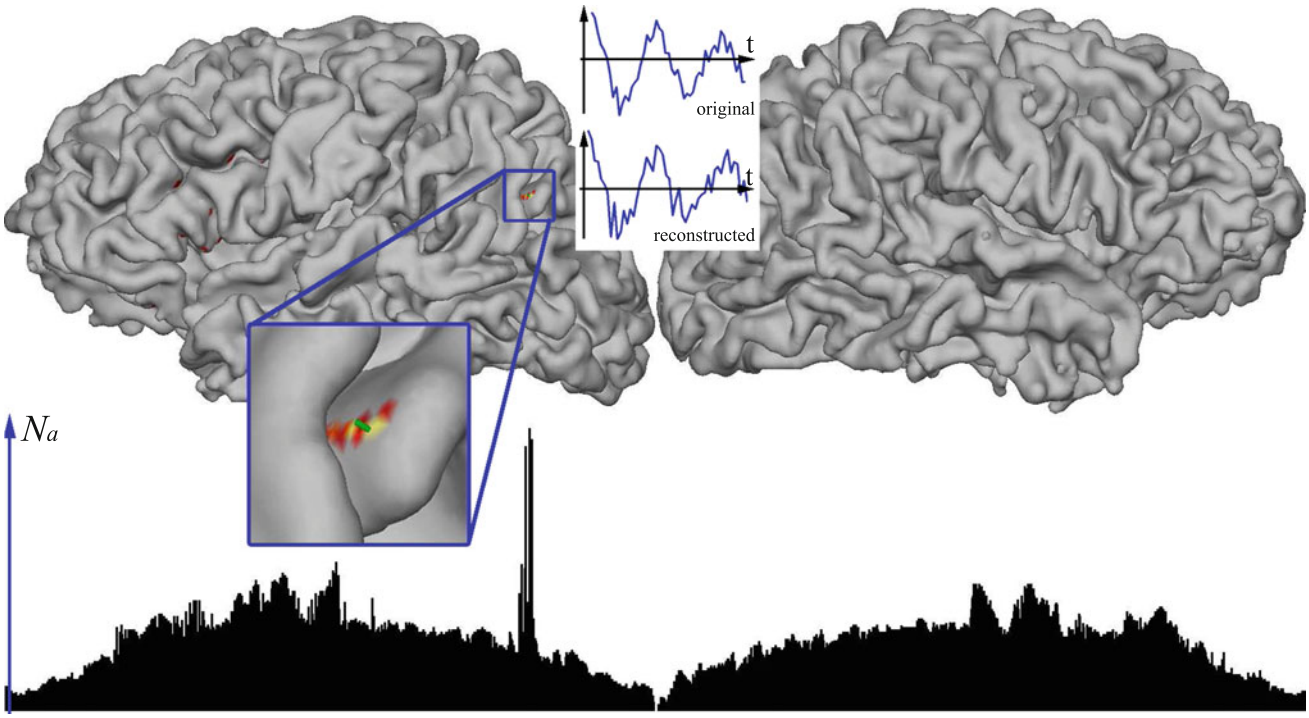

Fig. 6 Neural activity index: single dipole source. The time course of the source current (at the location in the left hemisphere as shown) is a damped oscillator with noise. The neural activity index N_a is plotted on the cortical surface (*top*) and as a function of the vertex coordinate in the longitudinal direction (*bottom*). The threshold for the values of N_a when plotted on the cortical surface is the average of N_a plus three standard deviations ($\bar{N}_a + 3\sigma$)

and how the detected activity is spread out in the space surrounding the source. Neural activity index values are plotted color coded (with a threshold to remove the noise) on the cortical surface (top), and blow-ups are provided for better visualization of the detected local activity around the dipole.

The neural activity index in Fig. 6 has a single sharp spike, which corresponds to the location of the dipole source in the left hemisphere, and a series of smaller spikes corresponding to sources with a similar forward solution. The reconstructed time series is plotted below the original and reproduces the damped oscillatory function and its frequency.

Figure 7 shows examples of the neural activity index, calculated from a simulated EEG dataset using two (a) and three (b) dipoles as main sources of the electric activity superimposed with the randomly activated locations on the cortical surface. The time series of the source dipoles are damped oscillators with noise and a phase shift. Since the beamforming algorithm is based on the calculation of the covariance matrix of the signal from the EEG electrodes, the activity index will likely fail to distinguish between source locations if any of the dipoles' dynamics have strong temporal correlations. This is especially the case for dipoles that are spatially close and/or parallel sources. For three dipoles, it is not sufficient to introduce another shift of the oscillatory time series, because in that case, one of the damped sinusoidal functions can always be represented as a linear combination of the other two and the neural activity index will only be able to detect two out of three locations. Therefore, in order to create uncorrelated sources, we use a different frequency for one of the source dipoles. An example with three dipoles is shown in Fig. 7b. The neural activity index shows three regions of activity, and the time series are reconstructed accurately.

As a next step in the beamformer simulations, we assume certain regions on the cortical surface, modeled by a number of dipoles, to be activated with the same time course for all sources within the patch. For example, if we consider a dipole in the left hemisphere and all its nearest neighbors, then a total of nine dipoles will form a patch and have the same dynamics. The neural activity index in Fig. 8 is calculated on a simulated EEG set, using two patches of nine dipoles each. We found that the highest value corresponds to the center of the patch, which implies that the sources surrounding the center dipole amplify the signal from the center of the patch. The time series of each of the nine dipole sources within each patch after reconstruction shows that the dynamical behavior is close to the original damped oscillator with noise.

EEG beamforming: realistic versus spherical head models

For a comparison of the different head models, we calculated EEG forward solutions for all three methods mentioned before: single-sphere, multi-sphere, and boundary element method. Figure 9 shows examples of forward solutions for a single dipole source in the left hemisphere for the different models. The single-sphere model, shown in Fig. 9a, does not take the conductivity of the skull into account and, as a result, provides a more localized distribution of the electric potential compared to the other models and due to its assumptions is unable to provide realistic results. Figures 9b and 9c represent forward solutions calculated for the concentric spheres geometry but using two different methods: infinite sum and boundary elements. As can be seen from the graphs and also verified by quantitative comparison, these two methods provide identical results. The boundary element method applied to the realistic geometry, shown in Fig. 9d, not only gives a more realistic EEG forward solution but also improves the accuracy of the beamforming source reconstruction when compared to spherical models. This can be demonstrated by using the spherical forward solutions to calculate the beamformer weights from a dataset created with the realistic geometry model. When using spherical models, the regions that are expected to be more or less accurate are the frontal and occipital lobes as they are at similar distances to the skull surface in both spherical and realistic geometries. On the other hand, since the brain is not spherical, the temporal lobes are expected to be the source of the largest error. Figure 10a shows the activity estimated using spherical beamforming on a realistic EEG signal and the source appears to be widespread. For comparison, realistic geometry beamforming, as shown in Fig. 10b, provides a much more localized estimate.

EEG beamforming: radial sources

An important practical advantage of EEG beamforming can be seen by investigating how source reconstruction is affected by the location and orientation of the source. To this end, we compare EEG versus MEG beamforming applied to both radial and tangential sources. The results are shown in Fig. 11, where it is evident that EEG beamforming analysis detects strong activity coming from both source locations. In contrast, MEG beamforming is only capable of detecting the tangential source. This result suggests that EEG beamforming may become a valuable addition to MEG and fMRI source localization methods.

Moreover, the plot of the EEG neural activity index in Fig. 11 shows that the radial source is localized with higher accuracy compared to the tangential source. This is due to the fact that EEG is most sensitive to currents located on top of gyri as shown earlier in Fig. 2, i.e., to the sources closest to the surface of the skull, the directions of which are mostly radial. Radial sources produce higher values of the electric potential on the scalp surface and therefore

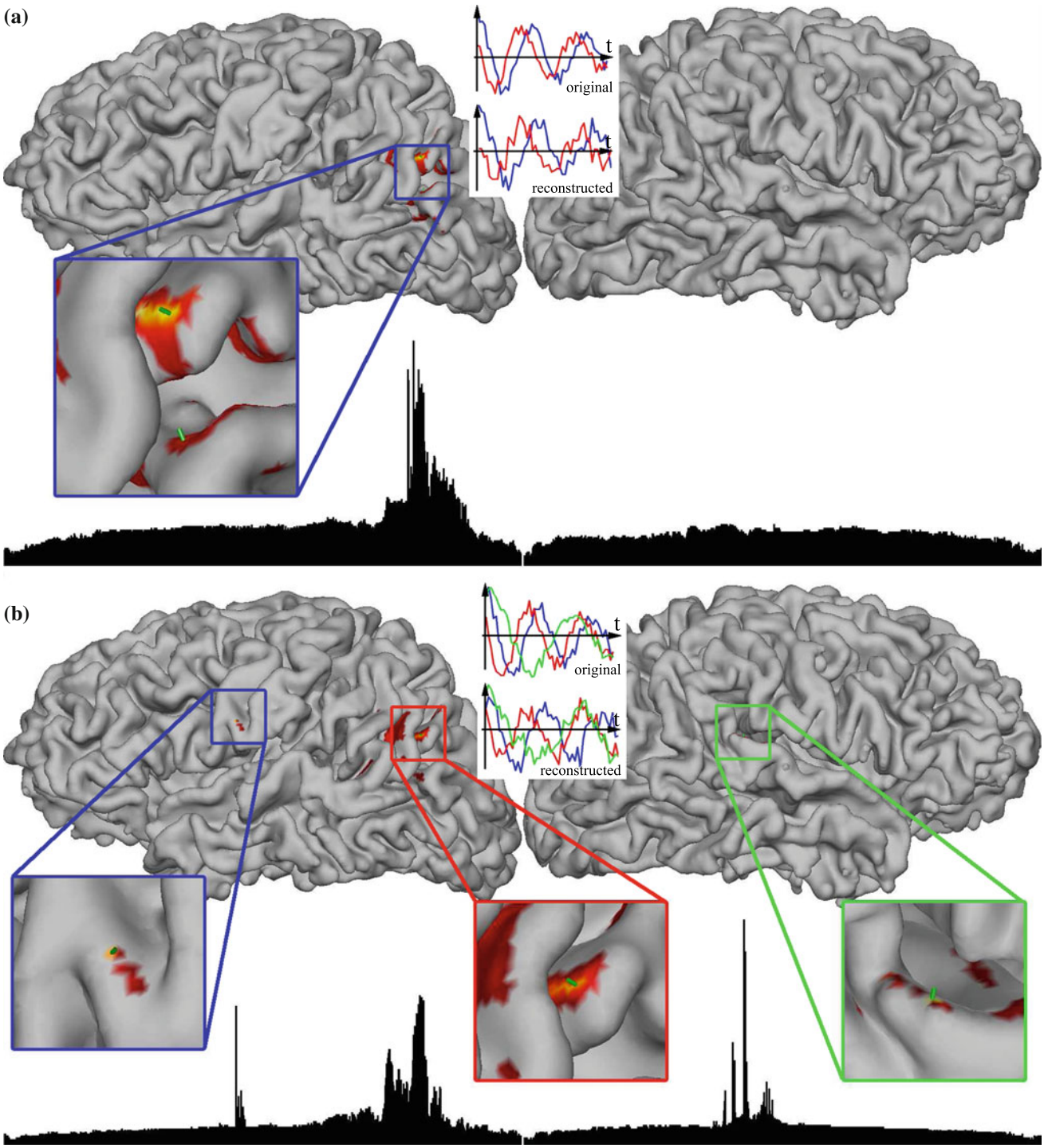

Fig. 7 Neural activity index: two (**a**) and three (**b**) dipole sources. The time courses feature phase and frequency shifts. The neural activity index is plotted on the cortical surface and as a function of the vertex coordinate in the longitudinal direction (below in *black*). The threshold for the values of N_a when plotted on the cortical surface is the average of N_a plus three standard deviations ($\bar{N}_a + 3\sigma$)

have a higher magnitude of the forward solution, which leads to a better signal-to-noise ratio. In addition, the electric potential created by tangential currents takes a path almost parallel to the skull (Nunez and Srinivasan 2006), which causes higher angular deflection and the potential on the scalp to be more smeared out and attenuated. This set of conditions renders radial currents more favorable for EEG beamforming and the activity index more accurate.

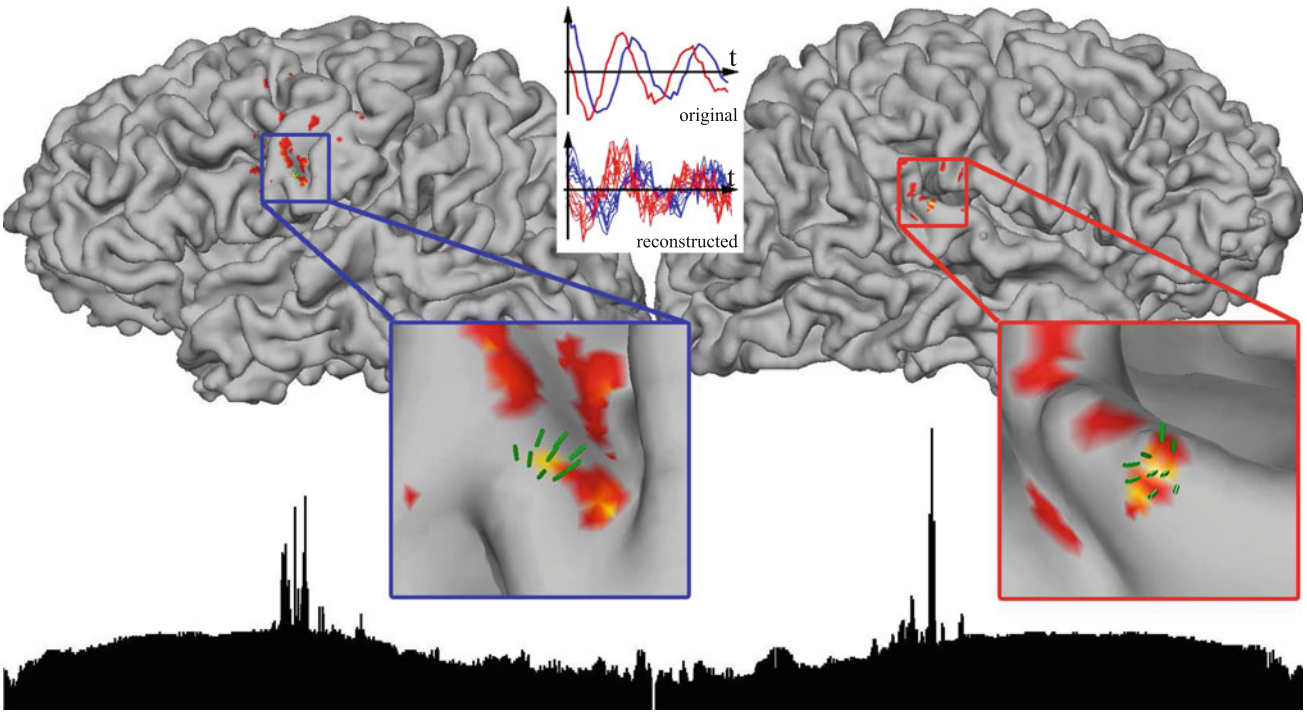

Fig. 8 Neural activity index: two patches of nine source dipoles. The time course for all dipoles within a patch is a damped oscillator with noise. Time courses between the patches are different by a phase shift of $\pi/2$ rad. The threshold for the values of N_a when plotted on the cortical surface is the average of N_a plus three standard deviations ($\bar{N}_a + 3\sigma$)

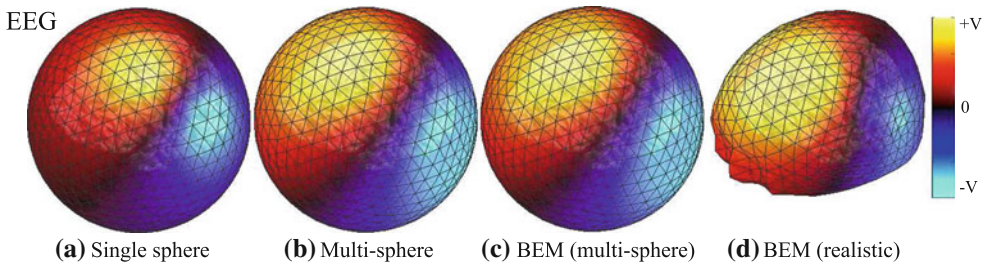

Fig. 9 Comparison of EEG forward solutions for different head models with a dipolar current source in the left hemisphere. Forward solutions are calculated using (**a**) single-sphere model, (**b**) multi-sphere model, and the boundary element method (BEM) applied to both multi-sphere (**c**) and realistic geometries (**d**)

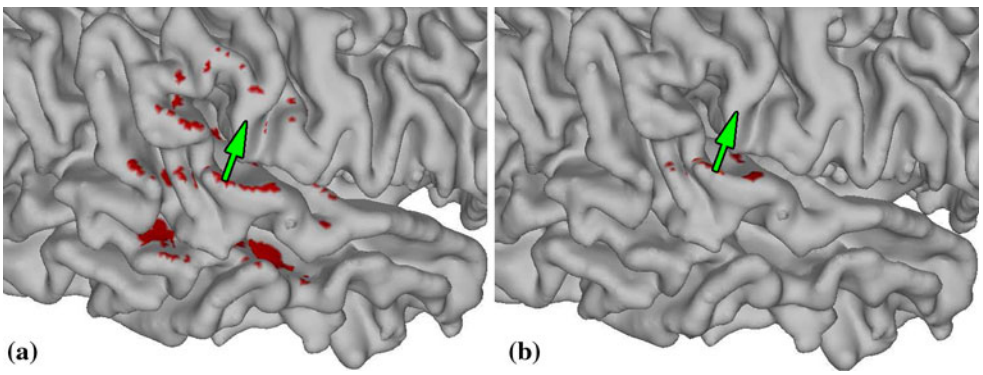

Fig. 10 Comparison of the electric activity (*red*) detected from a single source (*green arrow*) when multi-spherical (**a**) and realistic geometry (**b**) forward solutions are used. The realistic geometry model offers a more accurate source reconstruction

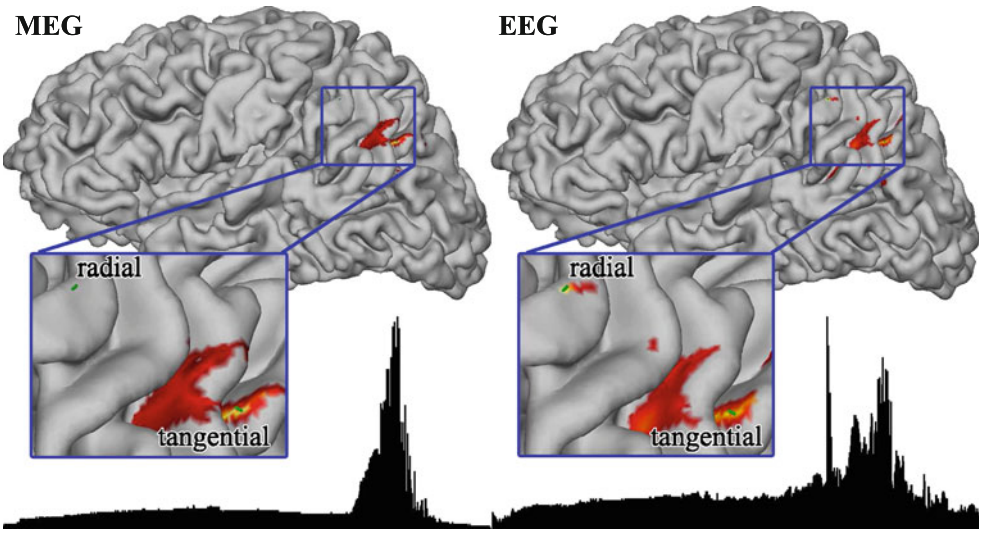

Fig. 11 Neural activity index: MEG beamforming versus EEG beamforming. MEG is insensitive to the radial source. The neural activity index is plotted on the cortical surface and as a function of the vertex coordinate in the longitudinal direction (*bottom*). The threshold for the values of N_a when plotted on the cortical surface is the average of N_a plus three standard deviations ($\bar{N}_a + 3\sigma$)

A good way to quantify the accuracy of the source reconstruction is receiver operating characteristic (ROC) analysis. The ROC is a graph of sensitivity (true positive rate) versus 1-specificity (false positive rate) and is widely used for evaluating and comparing different models as well as for determining the cutoff values for classification criteria. Figure 12 shows ROC curves for EEG and MEG beamforming (Darvas et al. 2004). These curves were calculated by applying the beamforming algorithm to 1,000 simulated EEG (MEG) data sets, each of which was based on a single dipole source randomly positioned on the cortical surface. Then, we apply a global threshold (measured in multiples of the standard deviation from the mean) to the neural activity index from each of these simulations, which defines the number of positives and negatives. The ROC curves are then obtained by varying the threshold and recording the corresponding true positive and false positive rates. As can be seen, the area under the EEG curve is close to 1, which means that all but a few sources are identified correctly, while in the MEG curve the false positive rate starts to increase around a true positive rate of 0.75, which means that about 25% of the dipoles (mostly radial sources) are below the noise level and could not be detected. The ROC analysis justifies our choice of the threshold for plotting the neural activity index $\bar{N}_a + 3\sigma$, which leads to a false positive rate smaller than 5% or $P < 0.05$.

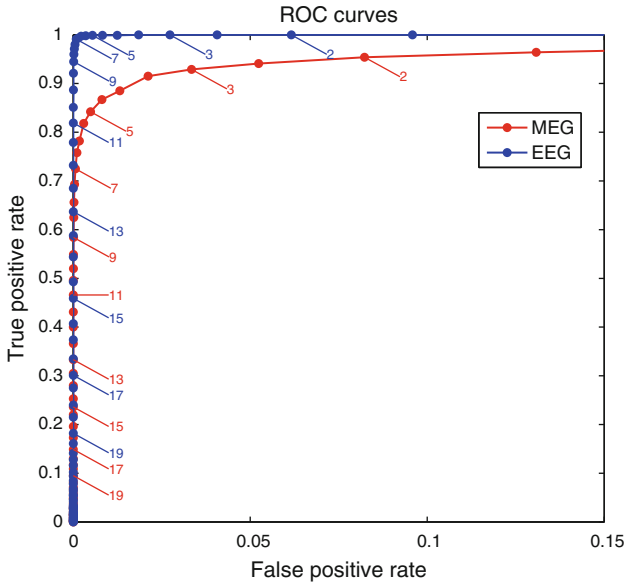

Fig. 12 Receiver operating characteristic (ROC) curves. The numbers represent the global threshold of the neural activity index measured in multiples of standard deviation from the mean. See text for details

Conclusions

The present research adopts a comprehensive approach to localizing distributed sources of neural activity and their dynamics in EEG signals by merging together a number of techniques such as beamforming, realistic geometry forward solutions, and cortical constraints. EEG source reconstruction accuracy is significantly affected by the blurring of the electric potential when passing through the skull. This is especially the case in EEG beamforming, where an accurate forward solution is important. Spherical head models, popular in many applications because of fast processing speeds, do not take the shape and thickness of the head tissues into account. To address this issue, we created a realistic multi-shell head model from CT scans, which allows for the EEG forward solution to be calculated using a boundary element method. Beamforming based on the BEM forward solution becomes computationally expensive for spatial resolution of the source reconstruction approaching 1 mm and requires additional assumptions to be made.

The neural sources that are known to be the generators of the EEG and MEG are concentrated in the cortical gray matter. Using MRI scans, we extracted the cortical surface and constrained all potential current sources, modeled as dipoles, to the surface of the gray-white matter interface. Imposing these anatomical constraints allows to reduce the dimensionality and to improve the spatial resolution of source reconstruction without major increase in computation time. The proposed technique was tested with different source configurations. EEG data were simulated at every point in time by superimposing the forward solutions from the main sources (dipoles with a damped oscillatory amplitude) and randomly active dipoles across the brain surface. In the analysis shown in Figs. 6, 7 and 8, we demonstrated the performance of the EEG beamformer in configurations of one, two, and three dipoles, and when the neural activity was spatially extended. Moreover, we also showed that the temporal dynamics of the sources can be reconstructed, revealing the original damped oscillatory behavior. Finally, we compared MEG and EEG beamforming and confirmed that in contrast to MEG, EEG allows for a detection of radial sources. The results of this work allow us to conclude that the proposed anatomically constrained beamforming procedure along with realistic geometry and conductivity-based forward solutions provides a viable and quite accurate approach to the inverse problem in EEG.

Acknowledgments This work was supported by NIMH grant 080838 and NINDS grant 48299 (JASK). The authors would like to thank Dr. Douglas Cheyne for helpful discussions. An earlier version of this research was presented as a poster (687.9) at the Society for Neuroscience meeting held in Chicago, IL, October 17-21, 2009.

Appendix 1: MEG forward solution

For locations outside, a spherical conductor the magnetic field can be calculated according to Sarvas (1987)

$$\boldsymbol{B}(\boldsymbol{r}) = \frac{\mu_0}{4\pi F^2(\boldsymbol{r},\boldsymbol{r}_q)}\{F(\boldsymbol{r},\boldsymbol{r}_q)\boldsymbol{q}\times\boldsymbol{r}_q - [\boldsymbol{q}\times\boldsymbol{r}_q\cdot\boldsymbol{r}]\nabla F(\boldsymbol{r},\boldsymbol{r}_q)\} \tag{5}$$

where $\boldsymbol{r}$ and $\boldsymbol{r}_q$ are the sensor and source locations, respectively, and $\boldsymbol{q}$ is the dipole direction as shown in Fig. 13. The scalar function $F(\boldsymbol{r}, \boldsymbol{r}_q)$ and its gradient $\nabla F(\boldsymbol{r}, \boldsymbol{r}_q)$ are given by

$$F(\boldsymbol{r},\boldsymbol{r}_q) = d\left(rd + r^2 - \boldsymbol{r}_q\cdot\boldsymbol{r}\right) \tag{6}$$

$$\nabla F(\boldsymbol{r},\boldsymbol{r}_q) = \left(\frac{d^2}{r} + \frac{\boldsymbol{d}\cdot\boldsymbol{r}}{d} + 2d + 2r\right)\boldsymbol{r} - \left(d + 2r + \frac{\boldsymbol{d}\cdot\boldsymbol{r}}{d}\right)\boldsymbol{r}_q \tag{7}$$

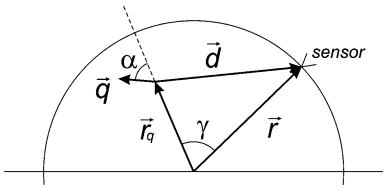

Fig. 13 Geometry of sensor and source: the source $\boldsymbol{q}$ is located at $\boldsymbol{r}_q$, the sensor is at $\boldsymbol{r}$. The angle between $\boldsymbol{q}$ and $\boldsymbol{r}_q$ is denoted as α, the angle between $\boldsymbol{r}$ and $\boldsymbol{r}_q$ as γ, and the angle between the planes formed by ($\boldsymbol{r}$, $\boldsymbol{r}_q$) and ($\boldsymbol{q}$, $\boldsymbol{r}_q$) is denoted as β (not shown). The vector from the dipole to the sensor is $\boldsymbol{d}$

It is commonly known that MEG has reduced sensitivity to radial sources (due to field cancelation by secondary currents) and is mostly generated by the sources located in the walls of cortical sulci. As can be seen, Sarvas' formula (Eq. 5) contains two cross-products $\boldsymbol{q}\times\boldsymbol{r}_q$, leading to $\boldsymbol{B}(\boldsymbol{r}) = \boldsymbol{0}$ for a radial source in a spherical conductor ($\boldsymbol{q}\|\boldsymbol{r}_q$) independent of sensor and source location.

Appendix 2: EEG forward solution

Single spherical conductor

For a single spherical conductor, the electric potential on the scalp at the sensor locations can be expressed in closed form (Mosher et al. 1999)

$$V_s(\boldsymbol{r},\boldsymbol{r}_q,\boldsymbol{q}) = \frac{q\cos\alpha}{4\pi\sigma}\left(\frac{2(r\cos\gamma - r_q)}{d^3} + \frac{1}{r_q d} - \frac{1}{r r_q}\right) + \frac{q\sin\alpha}{4\pi\sigma}\cos\beta\sin\gamma\left(\frac{2r}{d^3} + \frac{d+r}{rd(r - r_q\cos\gamma + d)}\right) \tag{8}$$

where the radius of the sphere is $r = |\boldsymbol{r}|$, the distance between the sensor at $\boldsymbol{r}$ and the dipole location at $\boldsymbol{r}_q$ is $d = |\boldsymbol{r} - \boldsymbol{r}_q|$ and the angles α, β and γ are as defined in Fig. 13.

Multi-sphere case

The multi-spherical forward solution requires the evaluation of an infinite sum (Zhang 1995) and the potential on the outermost (mth) surface reads

$$V_m(\boldsymbol{r},\boldsymbol{r}_q,\boldsymbol{q}) = \frac{q}{4\pi\sigma_m r^2}\sum_{n=1}^{\infty}\frac{2n+1}{n}\left(\frac{r_q}{r}\right)^{n-1} f_n \times \left\{n\cos\alpha P_n(\cos\gamma) + \cos\beta\sin\alpha P_n^1(\cos\gamma)\right\} \tag{9}$$

where P_n and P_n^1 are the Legendre and associated Legendre polynomials, respectively, and

$$f_n = \frac{n}{m_{22} + (1+n)m_{21}} \tag{10}$$

The coefficients m_{22} and m_{21} are found from

$$M = \begin{pmatrix} m_{11} & m_{12} \\ m_{21} & m_{22} \end{pmatrix} = \frac{1}{(2n+1)^{M-1}} \times \prod_{k=1}^{m-1} \begin{pmatrix} n + \frac{(n+1)\sigma_k}{\sigma_{k+1}} & (n+1)\left(\frac{\sigma_k}{\sigma_{k+1}} - 1\right)\left(\frac{r_q}{r_k}\right)^{2n+1} \\ n\left(\frac{\sigma_k}{\sigma_{k+1}} - 1\right)\left(\frac{r_k}{r_q}\right)^{2n+1} & (n+1) + \frac{n\sigma_k}{\sigma_{k+1}} \end{pmatrix} \tag{11}$$

In numerical calculations, the infinite series (Eq. 9) was found to converge before $n = 20$ and was truncated at this point. The matrices in Eq. 11 are non-commuting and the matrix with the highest index number is to be applied first, i.e., on the leftmost side. The most commonly used spherical multi-shell head model includes three layers: cerebrospinal fluid, skull, and scalp, which leads to $m = 3$.

Multi-shell case (realistic geometry)

The interfaces between the regions of different conductivity, as shown in Fig. 14, will be denoted by $S_1, \ldots, S_m$, with S_1 circumventing all the remaining surfaces, i.e., S_1 is the scalp. It can be shown that the electric potential V at $\boldsymbol{r} \in S_i$ obeys the Fredholm integral equation (Mosher et al. 1999)

$$(\sigma_i^- + \sigma_i^+)V(\boldsymbol{r}) = 2V_0(\boldsymbol{r}) + \frac{1}{2\pi}\sum_{j=1}^{m}(\sigma_j^- - \sigma_j^+) \int V(\boldsymbol{r}')d\Omega_{\boldsymbol{r}}(\boldsymbol{r}') \tag{12}$$

Here, the conductivities inside and outside the surface S_j are denoted by σ_j^- and σ_j^+, respectively. The solid angle $d\Omega_{\boldsymbol{r}}(\boldsymbol{r}')$ subtended at the location $\boldsymbol{r}$ by a surface element $\boldsymbol{dS}$ at $\boldsymbol{r}'$ is given by

$$d\Omega_{\boldsymbol{r}}(\boldsymbol{r}') = \frac{(\boldsymbol{r}' - \boldsymbol{r})}{|\boldsymbol{r}' - \boldsymbol{r}|^3} \cdot \boldsymbol{dS}_j(\boldsymbol{r}')$$

and

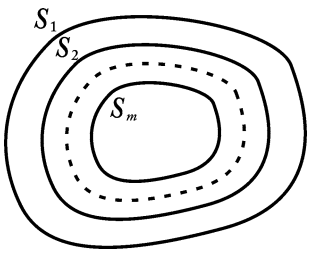

Fig. 14 Concentric multi-shell surfaces in the boundary element method. The surfaces are labeled from 1 (outermost) to m (innermost)

$$V_0(\boldsymbol{r}) = \frac{1}{4\pi\sigma_0}\int d^3r' \frac{\nabla' \cdot \boldsymbol{j}(\boldsymbol{r}')}{|\boldsymbol{r}' - \boldsymbol{r}|}$$

is the potential caused by the current $\boldsymbol{j}$ in an infinite homogeneous medium with conductivity $\sigma = 1$. To solve (Eq. 12) numerically, the surfaces S_i are divided into triangles Δ_k^i, resulting in a set of linear equations

$$\mathbf{V}^i = \sum_{j=1}^{m} \mathbf{B}^{ij}\mathbf{V}^j + \mathbf{g}^i \,; i = 1, \ldots, m \tag{13}$$

where the matrices $\mathbf{V}^i$, $\mathbf{g}^i$, and $\mathbf{B}^{ij}$ are defined by

$$\begin{aligned} V_k^i &= \frac{1}{\mu_k^i}\int_{\Delta_k^i} V(\boldsymbol{r})dS_i \\ g_k^i &= \frac{1}{\mu_k^i}\frac{2}{\sigma_i^- + \sigma_i^+}\int_{\Delta_k^i} V_0(\boldsymbol{r})dS_i \\ B_{kl}^{ij} &= \frac{1}{2\pi}\frac{1}{\mu_k^i}\Gamma_{ij}\int_{\Delta_k^i} \Omega_{\Delta_l^j}(\boldsymbol{r})dS_i \end{aligned} \tag{14}$$

Here i and j are the index numbers of the surfaces and k and l are the index numbers of the triangles on the surfaces. In addition, μ_k^i is the area of the kth triangle Δ_k^i on the surface S_i and $\Omega_{\Delta_l^j}$ is the solid angle subtended by the triangle Δ_l^j at the position of the center of the triangle Δ_k^i. For $k = l$ and $i = j$ we have $\Omega_{\Delta_l^j} = 0$. The number of triangles on each surface S_j is denoted by n_j and $\sum_{j=1}^{m} n_j = N$. The multipliers Γ_{ij} are given by

$$\Gamma_{ij} = \frac{\sigma_j^- - \sigma_j^+}{\sigma_i^- + \sigma_i^+} \tag{15}$$

We consider a three-layer head model with surfaces S_i, where $i = 1$ for the scalp, $i = 2$ for the skull, and $i = 3$ for the cerebrospinal fluid/brain. Now, we calculate the coefficients B_{kl}^{ij} in Eq. 14 using for the solid angle of a plane triangle (van Oosterom and Strackee 1983)

$$\Omega_{\Delta_l^j}(\boldsymbol{r}_{ck}^{\,i}) = \frac{2\boldsymbol{R}_1 \cdot (\boldsymbol{R}_2 \times \boldsymbol{R}_3)}{R_1R_2R_3 + (\boldsymbol{R}_1 \cdot \boldsymbol{R}_2)R_3 + (\boldsymbol{R}_1 \cdot \boldsymbol{R}_3)R_2 + (\boldsymbol{R}_2 \cdot \boldsymbol{R}_3)R_1} \tag{16}$$

with $R_i = |\boldsymbol{R}_i|$. The source g_k^i in Eq. 13 is defined by the dipole

$$g_k^i = \frac{1}{2\pi(\sigma_i^- + \sigma_i^+)}\sum_{r'} \frac{\nabla' \cdot \boldsymbol{j}(\boldsymbol{r}')}{|\boldsymbol{r} - \boldsymbol{r}'|}. \tag{17}$$

The solution of (Eq. 12) in the case of three surface layers can be represented by

$$V = \begin{pmatrix} \mathbf{V}^1 \\ \mathbf{V}^2 \\ \mathbf{V}^3 \end{pmatrix} = \begin{pmatrix} \mathbf{W}^1 \\ \mathbf{W}^2 \\ \mathbf{W}^3 + \mathbf{W}_0^3 \end{pmatrix} \tag{18}$$

where the term $\mathbf{W}_0^3$ has been added to avoid numerical problems and represents the potential on the surface of a homogeneous conductor bounded by surface S_3 (Hämäläinen and Sarvas 1989)

$$\mathbf{W}_0^3 = \left(\frac{\mathbf{B}^{33}}{\Gamma^{33}} - \frac{1}{n_3}\right)\mathbf{W}_0^3 + \frac{\sigma_3^- + \sigma_3^+}{\sigma_3^-}\mathbf{g}^3 \tag{19}$$

The unknown functions $\mathbf{W}^i$ can be found by solving the system of linear equations

$$\boldsymbol{W} = \begin{pmatrix} \mathbf{W}^1 \\ \mathbf{W}^2 \\ \mathbf{W}^3 \end{pmatrix} = \left(\mathbf{B}^{ij} - \frac{1}{n_1 + n_2 + n_3}\right)\boldsymbol{W} + \sigma_3^+ \begin{pmatrix} \mathbf{h}^1 \\ \mathbf{h}^2 \\ \mathbf{h}^3 \end{pmatrix} \tag{20}$$

where

$$\mathbf{h}^1 = \frac{\mathbf{g}^1}{\sigma_3^-}, \quad \mathbf{h}^2 = \frac{\mathbf{g}^2}{\sigma_3^-}, \quad \mathbf{h}^3 = \frac{\mathbf{g}^3}{\sigma_3^-} - \frac{2}{\sigma_3^- + \sigma_3^+}\mathbf{W}_0^3$$

To solve (Eq. 19) for $\mathbf{W}_k^i$, we rewrite it in the form

$$\left\{\mathbf{I} - \frac{\mathbf{B}^{33}}{\Gamma_{33}} + \frac{1}{n_3}\right\}\mathbf{W}_0^3 = \frac{\sigma_3^- + \sigma_3^+}{\sigma_3^-}\mathbf{g}^3 \tag{21}$$

where $\mathbf{I}$ is the identity matrix and the scalar $\frac{1}{n_3}$ is added to all elements of $\mathbf{I} - \frac{\mathbf{B}^{33}}{\Gamma_{33}}$. The solution of this system of linear equations together with the set of equations (Eq. 20) is then used to find the unknown vector $\boldsymbol{W}$

$$\left\{\mathbf{I} - \mathbf{B}^{ij} + \frac{1}{n_1 + n_2 + n_3}\right\}\boldsymbol{W} = \sigma_3^+ \boldsymbol{h}. \tag{22}$$

Numerical calculations start with the geometry matrix $\mathbf{B}^{ij}$ in (Eq. 14). The time to calculate this matrix depends on the number of vertices in the tesselation and can be computationally expensive, but it has to be performed only once per subject. Then, a source dipole is placed inside the innermost volume, and the potential on all three surfaces is calculated using (Eq. 18).

Appendix 3: Linearly constrained minimum variance (LCMV) beamforming

MEG or EEG data from an array of sensors can be represented by a time dependent vector $\mathbf{X}(t)$. In LCMV beamforming (Frost III 1972; van Veen and Buckley 1988), the signal $S_\Theta(t)$ measured by $\mathbf{X}(t)$ that originates from a source at Θ is given by $S_\Theta(t) = \mathbf{H}_\Theta \cdot \mathbf{X}(t)$ where $\Theta = (x, y, z, \psi, \phi)$ is a 5-dimensional quantity, which represents the location and direction of the current source, and $\mathbf{H}_\Theta$ are the beamforming weights. The global source power originating from Θ reads

$$\begin{aligned} S_\Theta^2 &= \frac{1}{T}\int_0^T \{\mathbf{H}_\Theta \cdot \mathbf{X}(t)\}^2 dt \\ &= \frac{1}{T}\int_0^T dt\left\{\sum_{i=1}^M H_{\Theta i} X_i(t)\right\}^2 \\ &= \sum_{i=1}^M \sum_{j=1}^M H_{\Theta i} H_{\Theta j} \underbrace{\frac{1}{T}\int_0^T X_i(t) X_j(t) dt}_{C_{ij}} \end{aligned} \tag{23}$$

where i, j represent the index number of a sensor and C_{ij} is the correlation matrix. Using $\mathbf{C}$, the global source power originating from Θ can be written in the compact form

$$S_\Theta^2 = \sum_{i=1}^M \sum_{j=1}^M C_{ij} H_{\Theta i} H_{\Theta j} = \mathbf{H}_\Theta \cdot \mathbf{C}\mathbf{H}_\Theta. \tag{24}$$

The beamformer weights $\mathbf{H}_\Theta$ are determined such that the total power over a certain time span becomes a minimum under the constraint that the signal originating from Θ, the forward solution $\mathbf{G}_\Theta$ multiplied by the beamformer weights $\mathbf{H}_\Theta$, remains constant, i.e.,

$$S_\Theta^2 = \frac{1}{T}\int_0^T \{\mathbf{H}_\Theta \cdot \mathbf{X}(t)\}^2 dt = \mathbf{H}_\Theta \cdot \mathbf{C}\mathbf{H}_\Theta \rightarrow \min \tag{25}$$

with the constraint $S_\Theta = \mathbf{H}_\Theta \cdot \mathbf{G}_\Theta = 1$.

The problem (Eq. 25) is solved using the method of lagrange multipliers (Frost III 1972; Fuchs 2007), a well-known method from classical mechanics. To this end, we write the constraint as

$$\mathbf{H}_\Theta \cdot \mathbf{G}_\Theta - 1 = 0 \tag{26}$$

then, multiply it by a constant λ and add it to the global source power S_Θ^2

$$S_\Theta^2 = \sum_{i=1}^M \sum_{j=1}^M C_{ij} H_{\Theta i} H_{\Theta j} + \lambda\left\{\sum_{i=1}^M H_{\Theta i} G_{\Theta i} - 1\right\} \rightarrow \min \tag{27}$$

Now, the source power is minimized by taking the derivative of S_Θ^2 with respect to $\mathbf{H}_\Theta$ and solve

$$\frac{\partial S_\Theta}{\partial H_{\Theta k}} = 2\sum_{i=1}^M C_{ik} H_{\Theta i} + \lambda G_{\Theta k} = 0 \tag{28}$$

for $\mathbf{H}_\Theta$. Equation 28 in matrix form reads

$$2\mathbf{C}\mathbf{H}_\Theta = -\lambda \mathbf{G}_\Theta \tag{29}$$

which results in

$$\mathbf{H}_\Theta = -\frac{\lambda}{2}\mathbf{C}^{-1}\mathbf{G}_\Theta. \quad (30)$$

The unknown Lagrange multiplier is found by using the constraint (Eq. 26) again, leading to

$$\left[-\frac{\lambda}{2}\mathbf{C}^{-1}\mathbf{G}_\Theta\right]\cdot\mathbf{G}_\Theta = 1 \quad \text{or} \quad \lambda = -2\left[\mathbf{G}_\Theta\cdot\mathbf{C}^{-1}\mathbf{G}_\Theta\right]^{-1} \quad (31)$$

Now, (Eq. 31) is inserted into the solution (Eq. 30) and the beamformer coefficients obtained as

$$\mathbf{H}_\Theta = \frac{\mathbf{C}^{-1}\mathbf{G}_\Theta}{\mathbf{G}_\Theta\cdot\mathbf{C}^{-1}\mathbf{G}_\Theta} \quad (32)$$

along with the global source power

$$S^2_\Theta = \mathbf{H}_\Theta\cdot\mathbf{C}\mathbf{H}_\Theta = \left[\mathbf{G}_\Theta\cdot\mathbf{C}^{-1}\mathbf{G}_\Theta\right]^{-1} \quad (33)$$

The so-called global neural activity index N_a is then calculated for every location and direction Θ and serves as a relative measure of activity originating from Θ. N_a can be calculated in different ways as distinguished by Huang et al. (2004). According to this classification, we used the type III activity index, defined as

$$N_a = \frac{\mathbf{G}_\Theta\cdot\mathbf{C}^{-1}\mathbf{G}_\Theta}{\mathbf{G}_\Theta\cdot\mathbf{C}^{-1}\mathbf{\Sigma}\mathbf{C}^{-1}\mathbf{G}_\Theta} \quad (34)$$

where $\mathbf{\Sigma}$ is the covariance matrix of the noise. $\mathbf{\Sigma}$ can be estimated from baseline data or chosen as a constant times the identity matrix.

References

Borgiotti G, Kaplan L (1979) Superresolution of uncorrelated interference sources by using adaptive array techniques. IEEE Trans Ant Prop 27:842–845

Braitenberg V, Schüz A (1991) Cortex: statistics and geometry of neural connectivity. Springer, Berlin

Brookes M, Mullinger K, Stevenson C, Morris P, Bowtell R (2008) Simultaneous EEG source localisation and artifact rejection during concurrent fMRI by means of spatial filtering. NeuroImage 40:1090–1104

Cheyne D, Gaetz W (2003) Neuromagnetic localization of oscillatory brain activity associated with voluntary finger and toe movements. NeuroImage 19(suppl):1061

Cheyne D, Bakhtazad L, Gaetz W (2006) Spatiotemporal mapping of cortical activity accompanying voluntary movements using an event-related beamforming approach. Hum Brain Mapp 27:213–229

Dale A, Fischl B, Sereno M (1999) Cortical surface-based analysis I: segmentation and surface reconstruction. NeuroImage 9:179–194

Darvas F, Pantazis D, Kucukaltun-Yildirim E, Leahy RM (2004) Mapping human brain function with MEG and EEG: methods and validation. NeuroImage 23(suppl 1):289–299

Delorme A, Makeig S (2004) EEGLAB: an open source toolbox for analysis of single-trial EEG dynamics. J Neurosci Methods 134:9–21

Fischl B, Sereno M, Dale A (1999) Cortical surface-based analysis II: inflation, flattening and a surface-based coordinate system. NeuroImage 9:194–207

Frost O III (1972) An algorithm for linearly adaptive array processing. Proc IEEE 60:926–935

Fuchs A (2007) Beamforming and its applications to brain connectivity. In: Jirsa VK, McIntosh AR (eds) Handbook of brain connectivity. Springer, Berlin, pp 357–378

Gorodnitsky I, Rao B, George J (1992) Source localization in magnetoencephalography using an iterative weighted minimum norm algorithm. In: Proceedings of the 26th Asilomar conference on signals, systems and computers, Pacific Grove, CA 92:167–171

Hämäläinen M, Ilmoniemi R (1994) Interpreting magnetic fields of the brain: minimum norm estimates. Med Biol Eng Comput 32:35–42

Hämäläinen M, Sarvas J (1989) Realistic conductivity geometry model of the human head for interpretation of neuromagnetic data. IEEE Trans Biomed Eng 36:165–171

von Helmholtz H (1853) Some laws concerning the distribution of electric currents in volume conductors with applications to experiments on animal electricity. Proc IEEE, translated by DB Geselowitz (2004) 92:868–870

van Hoey G, van de Walle R, Vanrumste B, d'Have M, Lemahieu I, Boon P (1999) Beamforming techniques applied in EEG source analysis. IEEE Proc ProRISC 10:545–549

Huang M, Shih J, Lee R, Harrington D, Thoma R, Weisend M, Hanion F, Paulson K, Li T, Martin K, Miller G, Canive J (2004) Commonalities and differences among vectorized beamformers in electromagnetic source imaging. Brain Topogr 16:139–158

Mosher J, Lewis P, Leahy R (1992) Multiple dipole modeling and localization from spatio-temporal MEG data. IEEE Trans Biomed Eng 39:541–557

Mosher J, Leahy R, Lewis P (1999) EEG and MEG: forward solutions for inverse methods. IEEE Trans Biomed Eng 46:245–259

Nunez P, Srinivasan R (2006) Electric fields of the brain. The neurophysics of EEG. 2nd edn. Oxford University Press, New York

van Oosterom A, Strackee J (1983) The solid angle of a plane triangle. IEEE Trans Biomed Eng 30:125–126

Robinson S, Vrba J (1999) Functional neuroimaging by synthetic aperture magnetometry (SAM). In: Yoshimoto T, Kotani M, Kuriki S, Karibe H, Nakasato N (eds) Recent advances in biomagnetism. pp 302–305 Tohoku University Press, Sendai

Sarvas J (1987) Basic mathematical and electromagnetic concepts of the biomagnetic inverse problem. Phys Med Biol 32:11–22

Sekihara K (1996) Generalized Wiener estimation of three-dimensional current distribution from biomagnetc measurements. IEEE Trans Biomed Eng 43:281–291

Spencer M, Leahy R, Mosher J, Lewis P (1992) Adaptive filters for monitoring localized brain activity from surface potential time series. In: Proceedings of the 26th asilomar conference on signals, systems and computers, Pacific Grove, CA pp 156–161

Stok C, Meijs J, Peters M (1987) Inverse solutions based on MEG and EEG applied to volume conductor analysis. Phys Med Biol 32:99–104

van Veen B, Buckley K (1988) Beamforming: a versatile approach to spatial filtering. IEEE ASSP Mag 5:4–24

van Veen B, van Drongelen W, Yuchtman M, Suzuki A (1997) Localization of brain electrical activity via linearly constraint minimum variance spatial filtering. IEEE Trans Biomed Eng 44:867–880

Ward D, Jones R, Bones P, Carroll G (1998) Enhancement of epileptiform activity in the EEG by 3-D adaptive spatial filtering: simulations and real data. In: Proceedings of the 20th annual international conference of the IEEE engineering in medicine and biology society 20:2116–2119

Wong D, Gordon K (2009) Beamformer suppression of cochlear implant artifacts in an electroencephalography dataset. IEEE Trans Biomed Eng 56:2851–2857

Zhang Z (1995) A fast method to compute surface potentials generated by dipoles within multilayer anisotropic spheres. Phys Med Biol 40:335–349